Simulation of fluid flow and permeability in cohesionless soils

by

Nicos Martys
Building and Fire Research Laboratory
National Institute of Standards and Technology
Gaithersburg, MD 20899 USA

and

E. Masad and B. Muhunthan
Department of Civil and Environmental Engineering
Washington State University
Pullman, Washington USA

Reprinted from Water Resources Research, Vol. 36, No. 4, 851-864, April 2000

NIST
National Institute of Standards and Technology
Technology Administration, U.S. Department of Commerce

WATER RESOURCES RESEARCH, VOL. 36, NO. 4, PAGES 851–864, APRIL 2000

Simulation of fluid flow and permeability in cohesionless soils

E. Masad and B. Muhunthan

Department of Civil and Environmental Engineering, Washington State University, Pullman

N. Martys

Building and Fire Research Laboratory, National Institute of Standards and Technology, Gaithersburg, Maryland

Abstract. This paper reports on a new laboratory methodology for the determination of the structure of pores, a method for the analysis of the data to obtain the statistics of the pore structure distribution, simulation of porous media with statistics consistent with those in the specimens, numerical simulation of fluid flow in images of porous media, and the determination of permeabilities from the numerical experiments and comparison with the results of laboratory experiments. The computed flow fields show that flow in porous media is restricted to preferential paths depending on the size and connectivity of pores. Whole areas of the pore structure are relatively isolated from the flow because of bottlenecks. The distribution of the isolated regions depends on the angularity of the grains and the porosity of the medium. The more angular the grains are the greater is the possibility for the presence of isolated regions. For grains with the same angularity a decrease in the porosity leads to concentration of flow along preferential flow paths. The permeability tensor coefficients are derived from the flow fields of the two-dimensional images as well as the three-dimensional computer-simulated images of soil microstructure. The numerical values of permeability and permeability anisotropy ratio compare well with laboratory experimental data.

1. Introduction

The description of the continuous voids or pores is necessary to study the transport of fluids through cohesionless soil deposits. The pores are, however, disordered; that is, their size, cross-sectional shape, and orientation are highly variable from point to point. The physical characterization of the disorder of the system of pores in a porous medium is complex and remains formidable for a comprehensive solution. Attempts in the past have included characterization by grain size distribution and simulation by various types of models with equivalent hydrodynamic characteristics, such as bundles of straight tubes of constant cross section or tubes with varying sectional area and alignment but with an equivalent hydraulic radius. These, in turn, have been used in the development of permeability relations [e.g., *Kozeny*, 1927; *Childs and Collis-George*, 1950; *Carman*, 1956; *Bear*, 1972; *Dullien*, 1979; *Koplic et al.*, 1984; *Berryman and Blair*, 1986].

Recent advances in digital image processing have opened up new avenues to quantify and simulate the porous medium microstructure [*Adler et al.*, 1990; *Martys et al.*, 1994; *Masad and Muhunthan*, 2000]. The main focus of this paper is to present a full description of the steady flow of water in a two-dimensional (2-D) porous microstructure captured in a computer using image-processing techniques. It also presents a procedure for the simulation of the soil microstructure based on measurements of the statistics of the anisotropic pore space distribution. Measurements are obtained using image processing of soil microstructure.

This paper is organized as follows. Section 2 summarizes the preparation procedure of soil specimens for image analysis. It describes the resin-impregnation technique used to obtain plane sections of cohesionless soil specimens for microstructural observations.

Section 3 deals with the reconstruction of the three-dimensional (3-D) anisotropic cohesionless soil microstructure in a computer. The technique utilizes two statistical properties, namely, the mean porosity and the directional autocorrelation function of the soil specimen. These concepts and simulation of the statistics of the pore space are described herein.

Section 4 is devoted to the flow problem. The Navier-Stokes equations are discretized on a microscopic image by means of a finite difference scheme and solved under prescribed macroscopic pressure gradients. The global permeability of the soil medium is obtained by integration of the flow field. The numerical values of average permeability and permeability anisotropy ratio are compared with experimental data.

Paper number 1999WR900348.
0043-1397/00/1999WR900348$09.00

2. Image Analysis of Soil Specimens

Glass beads 1 mm in diameter, Ottawa 30-40 sand, and silica 30-40 sand, representing different grain shapes, were used in the study. The shape of the grains was determined by the average axial ratio $\bar{n}$, defined as the ratio of the apparent longest axis L_1 to the apparent shortest axis L_2 of two-dimensional projections of particles:

$$\bar{n} = \frac{1}{N} \sum_{i=1}^{N} \left(\frac{L_1}{L_2} \right)_i, \tag{1}$$

where N is the number of particles. The average values of axial ratio of glass beads, Ottawa sand, and silica sand were estimated based on measurements made on 100 particles of each material using image analysis software [*National Institutes of Health (NIH)*, 1992] and were found to be 1.00, 1.25, and 1.50,

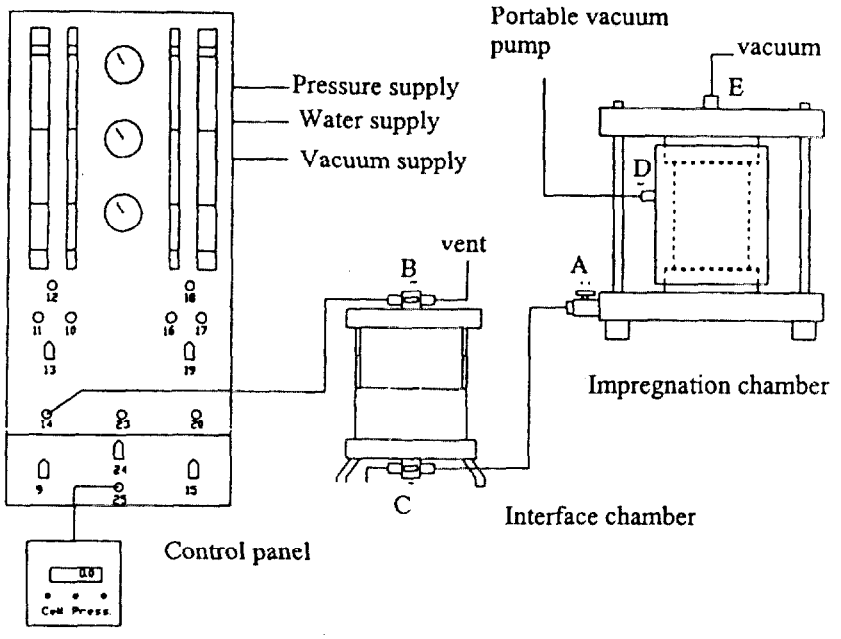

(a)

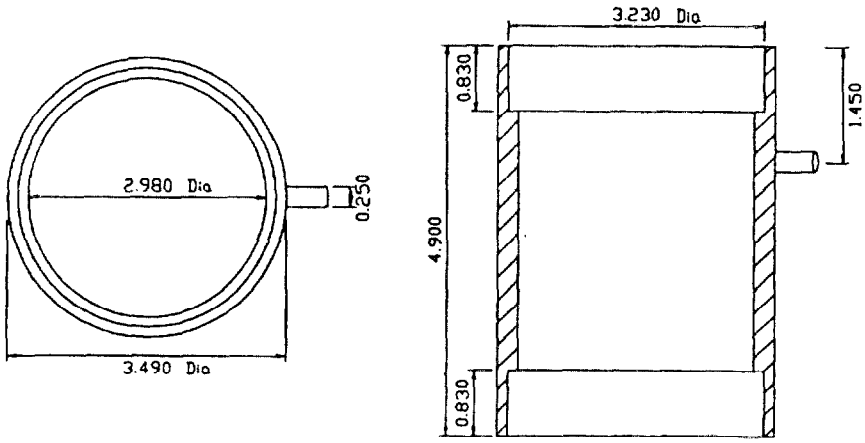

(b)

Figure 1. (a) Resin impregnation experimental setup. (b) Impregnation chamber.

respectively. It can be seen that the glass beads are spherical, Ottawa sand is composed mainly of subrounded grains, and silica sand is composed mainly of elongated grains.

Resin is often used as an impregnation material to facilitate hardening of sand and clay for preparation of sections for microscopic observations [*Kuo and Frost*, 1995; *Ibrahim and Kagawa*, 1991; *Smart and Tovey*, 1982]. Many of the impregnation techniques that are extant, however, provide little control over specimen confinement and time of impregnation.

Masad and Muhunthan [2000] have presented a detailed description of a new resin-impregnation apparatus which minimizes the resin-impregnation time and provides controlled confinement to the specimen to minimize the microstructure disturbance. It consists of three main components: a control panel, an interface chamber, and an impregnation chamber (Figure 1a). The control panel is used to regulate the applied pressure during resin impregnation. The interface chamber has two compartments separated by a membrane. The upper compartment is filled with water and is connected to the control panel. The lower compartment is filled with resin and is connected to the impregnation chamber. This feature enables the monitoring of the amount of resin impregnated into the spec-

imen since it is equal to the amount of water forced from the control panel burettes into the upper compartment of the interface chamber. In addition, it restricts resin from making contact with the control panel. This setup was used in this study to prepare sand specimens for microstructural analysis.

Two specimens from Ottawa 30-40 sand, one specimen from silica 30-40 sand, and one specimen from glass beads were prepared at porosity values of 0.42, 0.40, 0.45, and 0.36, respectively. The specimens were constructed inside the impregnation chamber (Figure 1b) using the dry pluviation technique [*Miura and Toki*, 1982]. This technique involves the uniform raining of sand from a constant height (5 cm) above the center of the specimen through a funnel with a predetermined opening size (4 mm).

Epo-thin resin manufactured by Buehler Ltd., Lake Bluff, Illinois, was used in this study. The resin was mixed with Epothin hardener manufactured by the same company and acetone as thinner to facilitate the impregnation process. The optimum mix proportion by weight of resin, hardener, and acetone was determined to be 100:40:8. This proportion was determined to allow the mixture to harden at room temperature and to adequately reduce the viscosity of the mixture. Reduction of the mixture viscosity minimizes specimen disturbance during impregnation. Negligible, if any, volume changes were recorded in specimens prepared using this mixture, indicating the minimum disturbance to the structure.

The completed specimens were cut into sections using an electric diamond saw following the pattern shown on Figure 2. The cut face of each section was polished using a diamond-lapping wheel. An ethanol-based fast green stain was applied to the polished faces to provide contrast between the solids and voids.

Image capturing was performed using an optical microscope linked to an image analyzer. Three images were obtained from the top of sections A, C, and E and from each of the four cut faces of sections B and D. That is, a total of 33 images were captured from each specimen. Image thresholding was performed to convert the gray-scale images to black (solids) and white (voids). Each image was square in shape and had a width h of 70 pixels in each direction.

The representative elementary volume reduces to the representative elementary area (REA) in 2-D analysis. The image area of sand that satisfied the REA criterion was found to be 5 mm × 5 mm, and the corresponding area was 10 mm × 10 mm for glass beads. Each image contained about 100–150 particles. The representative image length or width was equivalent to approximately 10 times the average grain diameter [*Masad and Muhunthan*, 2000].

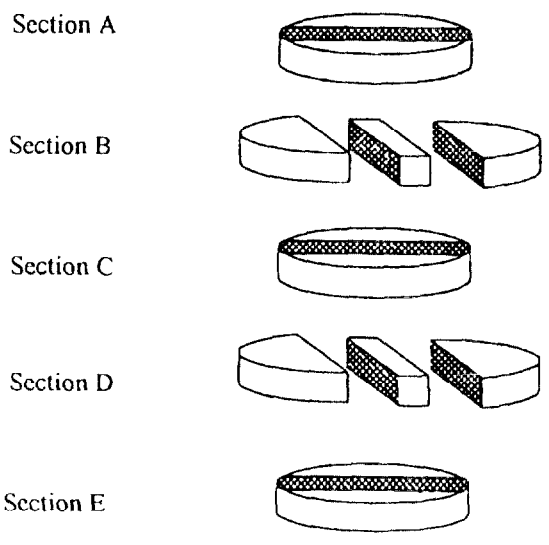

Figure 2. Cutting pattern of granular specimens.

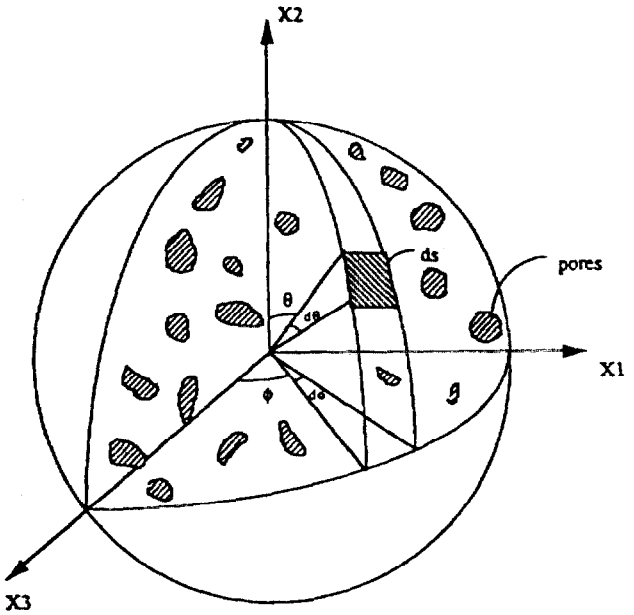

Figure 3. The coordinate system used in the analysis.

3. Reconstruction of Soil Microstructure

The reconstruction of the 3-D image of the anisotropic soil microstructure in the computer is accomplished by simulating an artificial medium with nearly identical statistical characteristics to the soil microstructure. The simulation can be done for both 2-D and 3-D images of soil microstructure.

The statistical properties used in the simulation are the average porosity and the directional autocorrelation function (DACF) [*Masad and Muhunthan*, 2000]. Both properties are measured from three orthogonal images captured on the resin-impregnated soil specimens. The average porosity is directly calculated using the image analysis system as the area of voids relative to the total area of an image [*NIH*, 1992].

The DACF is a function of the vector that separates any two points of the soil medium. The vector magnitude is denoted by r, while its direction is defined by the unit vector $\mathbf{l}$ ($l_1 = \sin\theta \sin\phi$, $l_2 = \cos\theta$, and $l_3 = \sin\theta \cos\phi$) (Figure 3). In order to capture the directional distribution of microstructure elements, the DACF is expressed by the spherical harmonic series in the Cartesian coordinate limited to the second order. The DACF at vector length r, $f_r(\mathbf{l})$, is given by

$$f_r(\mathbf{l}) = (f_a)_r(1 + \Omega_{mn} l_m l_n), \tag{2}$$

where $(f_a)_r$ is the average (isotropic) autocorrelation function at vector length r and Ω_{mn} is a component of the second-order deviatoric tensor. This tensor describes the deviation of the DACF from the average value in the direction of the unit vector $\mathbf{l}$. The experimental procedure for obtaining $(f_a)_r$ and Ω_{mn} for 2-D and 3-D cases is given by *Masad and Muhunthan* [1998].

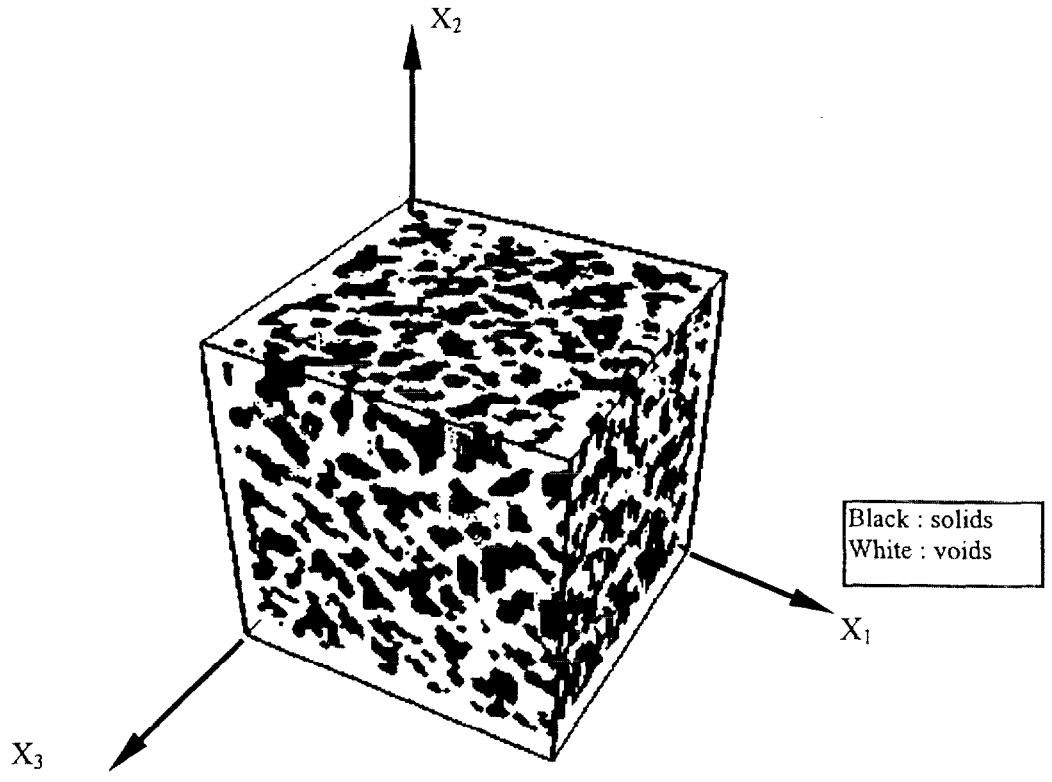

Figure 4. Three-dimensional section of the simulated structure of image set 2. The size is 50 × 50 × 50 voxels (3.5 mm × 3.5 mm × 3.5 mm).

The simulation procedure starts by creating a 3-D image of Guassian distributed noise [*Law and Kelton*, 1982; *Press and Teukolsky*, 1992]. Then, the noise image is filtered (or convolved) with the DACF $f_r(\mathbf{l})$ (equation (2)) to obtain another image that exhibits the anisotropy of the actual soil microstructure [*Masad and Muhunthan*, 1998]. This image is converted to a binary (0 (pore) or 1 (solid)) image using a threshold operation. The threshold value is determined such that the resulting 3-D image has the same porosity as the images captured on specimens. The total size of the reconstructed microstructure is 70 × 70 × 70 voxels (5 mm × 5 mm × 5 mm for sand and 10 mm × 10 mm × 10 mm for glass beads). An example of the reconstructed microstructure is given in Figure 4.

4. Simulation of Fluid Flow and Permeability

The incompressible fluid flow is governed by the following set of equations [*Bird et al.*, 1960]:

Continuity equation

$$\frac{\partial \rho u}{\partial x} + \frac{\partial \rho v}{\partial y} + \frac{\partial \rho w}{\partial z} = 0. \tag{3}$$

Navier-Stokes (momentum) equations in the x, y, and z directions, respectively,

$$u\frac{\partial \rho u}{\partial x} + v\frac{\partial \rho u}{\partial y} + w\frac{\partial \rho u}{\partial z} = -\frac{\partial p}{\partial x} + \frac{\partial}{\partial x}\left(\mu\frac{\partial u}{\partial x}\right) + \frac{\partial}{\partial y}\left(\mu\frac{\partial u}{\partial y}\right) + \frac{\partial}{\partial z}\left(\mu\frac{\partial u}{\partial z}\right) \tag{4}$$

$$u\frac{\partial \rho v}{\partial x} + v\frac{\partial \rho v}{\partial y} + w\frac{\partial \rho v}{\partial z} = -\frac{\partial p}{\partial y} + \frac{\partial}{\partial x}\left(\mu\frac{\partial v}{\partial x}\right) + \frac{\partial}{\partial y}\left(\mu\frac{\partial v}{\partial y}\right) + \frac{\partial}{\partial z}\left(\mu\frac{\partial v}{\partial z}\right) \tag{5}$$

$$u\frac{\partial \rho w}{\partial x} + v\frac{\partial \rho w}{\partial y} + w\frac{\partial \rho w}{\partial z} = -\frac{\partial p}{\partial z} + \frac{\partial}{\partial x}\left(\mu\frac{\partial w}{\partial x}\right) + \frac{\partial}{\partial y}\left(\mu\frac{\partial w}{\partial y}\right) + \frac{\partial}{\partial z}\left(\mu\frac{\partial w}{\partial z}\right), \tag{6}$$

where u, v, and w are the velocity in the x, y, and z directions, respectively, μ is the fluid viscosity, and ρ is the fluid density.

Several finite difference and finite element formulations have been developed in the past to provide solutions to these equations at the material microstructural level [*Adler et al.*, 1990; *Martys et al.*, 1994]. Most of them, however, were developed for isotropic distribution of the pores and make a priori assumptions about the significance of the viscous or convection (inertial) components of the Navier-Stokes equations depending on the problem under consideration.

The simulation of two-dimensional fluid flow in a saturated anisotropic soil medium is performed in this study by implementing a numerical solution to the complete set of Navier-Stokes equations at the soil microstructural level. The numerical solution does not make any a priori assumptions about the significance of the viscous or convection components. Therefore the program can be used to simulate fluid flow for a wide range of applications.

For 2-D incompressible flow the governing fluid flow equations reduce to

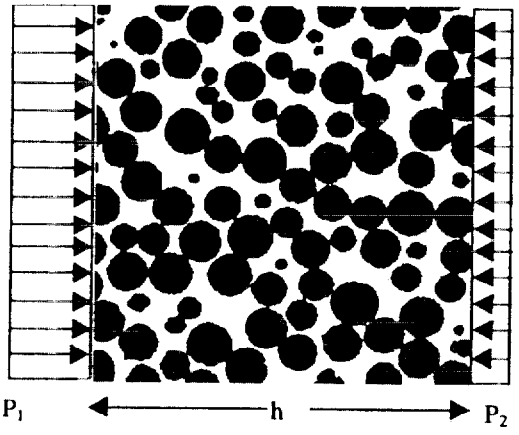

Figure 5. A typical image of glass beads used in permeability analysis.

$$\frac{\partial \rho u}{\partial x} + \frac{\partial \rho v}{\partial y} = 0 \tag{7}$$

$$\frac{\partial}{\partial x}\left(\rho u u - \mu \frac{\partial u}{\partial x}\right) + \frac{\partial}{\partial y}\left(\rho u v - \mu \frac{\partial u}{\partial y}\right) = -\frac{\partial p}{\partial x} + \frac{\partial}{\partial x}\left(\mu \frac{\partial u}{\partial x}\right) + \frac{\partial}{\partial y}\left(\mu \frac{\partial v}{\partial x}\right) \tag{8}$$

$$\frac{\partial}{\partial y}\left(\rho v v - \mu \frac{\partial v}{\partial y}\right) + \frac{\partial}{\partial x}\left(\rho v u - \mu \frac{\partial v}{\partial x}\right) = -\frac{\partial p}{\partial y} + \frac{\partial}{\partial y}\left(\mu \frac{\partial v}{\partial y}\right) + \frac{\partial}{\partial x}\left(\mu \frac{\partial u}{\partial y}\right), \tag{9}$$

where u and v are the velocity in x and y directions, respectively. Although the 2-D Navier-Stokes equations can be further simplified, the form presented in (8) and (9) facilitates their finite difference formulation and numerical solution. The staggered grid arrangement of the velocity and pressure nodes was used to discretize the fluid flow differential equations over the grid of two-dimensional images and develop the finite difference formulations of the governing equations at the soil microstructural level. The equations were solved numerically by using the general formulation known in computational fluid dynamics as semi-implicit method for pressure linked equations (SIMPLE) [*Patankar and Spalding*, 1970]. The complete derivation of the finite difference formulations for the microscopic images of soil specimens is given in the appendix, and a listing of the fluid flow simulation program is given by *Masad* [1998].

The flow equations were solved for actual images captured on the resin-impregnated soil specimens. A typical image of glass beads used in the analysis is shown in Figure 5. Velocity fields within an image are driven by a pressure difference $\Delta p = p_2 - p_1$ maintained between the inlet and the outlet of an image (Figure 5). The boundary conditions of velocity components are

$$u(x = 0) = u(x = h) \tag{10}$$

$$v(x = 0) = v(x = h) \tag{11}$$

$$u(y = 0) = u(y = h) \tag{12}$$

$$v(y = 0) = v(y = h) \tag{13}$$

and at the solid phase ("no slip" condition)

$$u = v = 0, \tag{14}$$

where h is the width of an image in pixels. Equations (10)–(13) represent periodic boundary conditions.

5. Flow Analysis Results

The flow field in a 2-D image of Ottawa sand is shown in Figure 6. The length of a vector at any point is the magnitude of velocity at that point. Notice that the fluid is forced to flow from left to right. In general, it can be seen that water flows in parallel lines within local regions. It is noted, however, that flow is highly irregular and not evenly distributed throughout the image. The flow path direction and shape depend on the

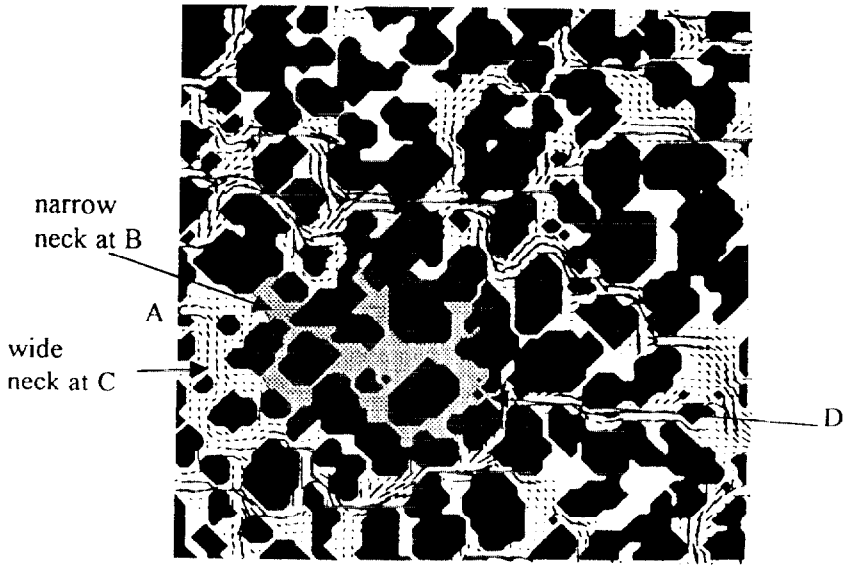

Figure 6. Simulation of two-dimensional (2-D) flow in an image of Ottawa sand. Size of an image is 50 × 50 × 50 pixels equal to 3.5 mm × 3.5 mm × 3.5 mm.

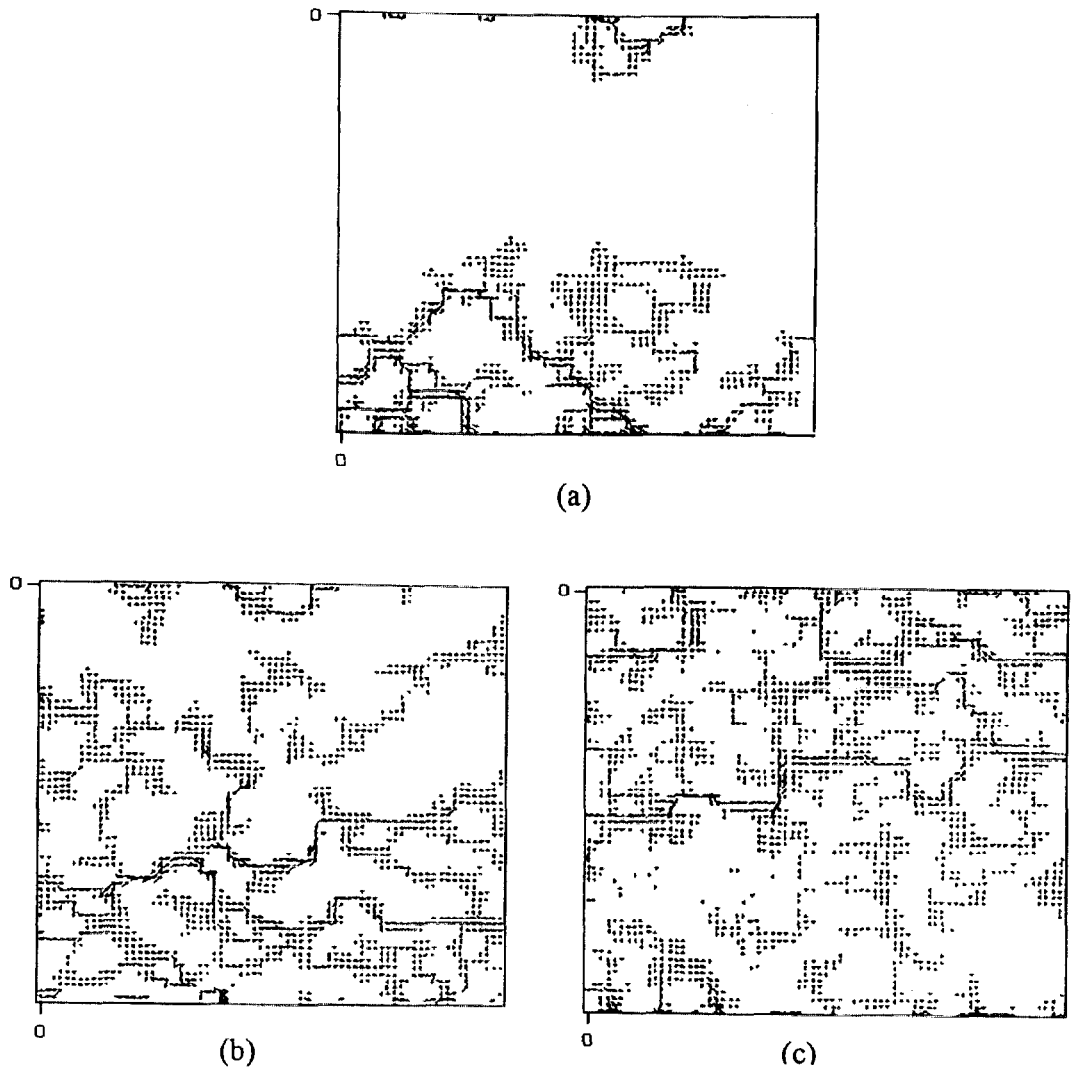

Figure 7. Flow fields in 2-D images of Ottawa sand at different porosity values: (a) 0.354, (b) 0.396, and (c) 0.460.

size of the voids and void connectivity. Figure 6 illustrates the effect of narrow necks that connect pores on water flow. In Figure 6, water enters from point A, and it has two paths to reach point D. The first path is through the narrow neck at point B, and the second one is through the wide neck at point C. The narrow neck at point B, however, controls the flow, such that water seeps through the wide neck at C following the A-C-D path. Consequently, very small velocities are observed in the A-B-D path represented by the shaded area (Figure 6). It is of interest to note that though relatively large sizes of pores are present in the shaded area, they do not contribute to fluid flow through the porous medium.

Figure 7 shows comparison of flow fields in Ottawa sand images at different porosities. It can be seen that as the porosity decreases, the flow becomes more concentrated along preferential paths. In addition, the flow field becomes more tortuous (follows longer paths) with decrease in porosity. It appears that as the percent of solids increases within an image, the particle contact increases, and the flow field picks out paths connected by large voids.

Figure 8 is a comparison of flow fields in three images captured from Ottawa sand, glass beads, and silica sand specimens. The images are chosen such that their porosity values are nearly identical (Figure 8). The flow, however, is more uniformly distributed in the glass bead image than in the Ottawa sand and silica sand images. Only one or two main paths carry the flow in silica sand. The silica sand image has more stagnant areas for fluid flow than Ottawa sand and glass beads. This is to be expected as silica sand has a much rougher surface and, consequently, higher specific surface area than the other two materials. As the surface area increases, solid particles become interlocked, and narrower necks are formed increasing resistance to flow. Water chooses the path with the least resistance to flow. Therefore the number of flow paths decreases with an increase in specific surface area.

5.1. Permeability Coefficient

The fluid permeability is defined via Darcy's law:

$$\bar{\mathbf{v}} = -\frac{1}{\mu}\,\mathbf{K}\cdot\nabla p, \tag{15}$$

where $\bar{\mathbf{v}}$ is average velocity vector within a sample, μ is the viscosity coefficient, ∇p is a prescribed pressure gradient, and

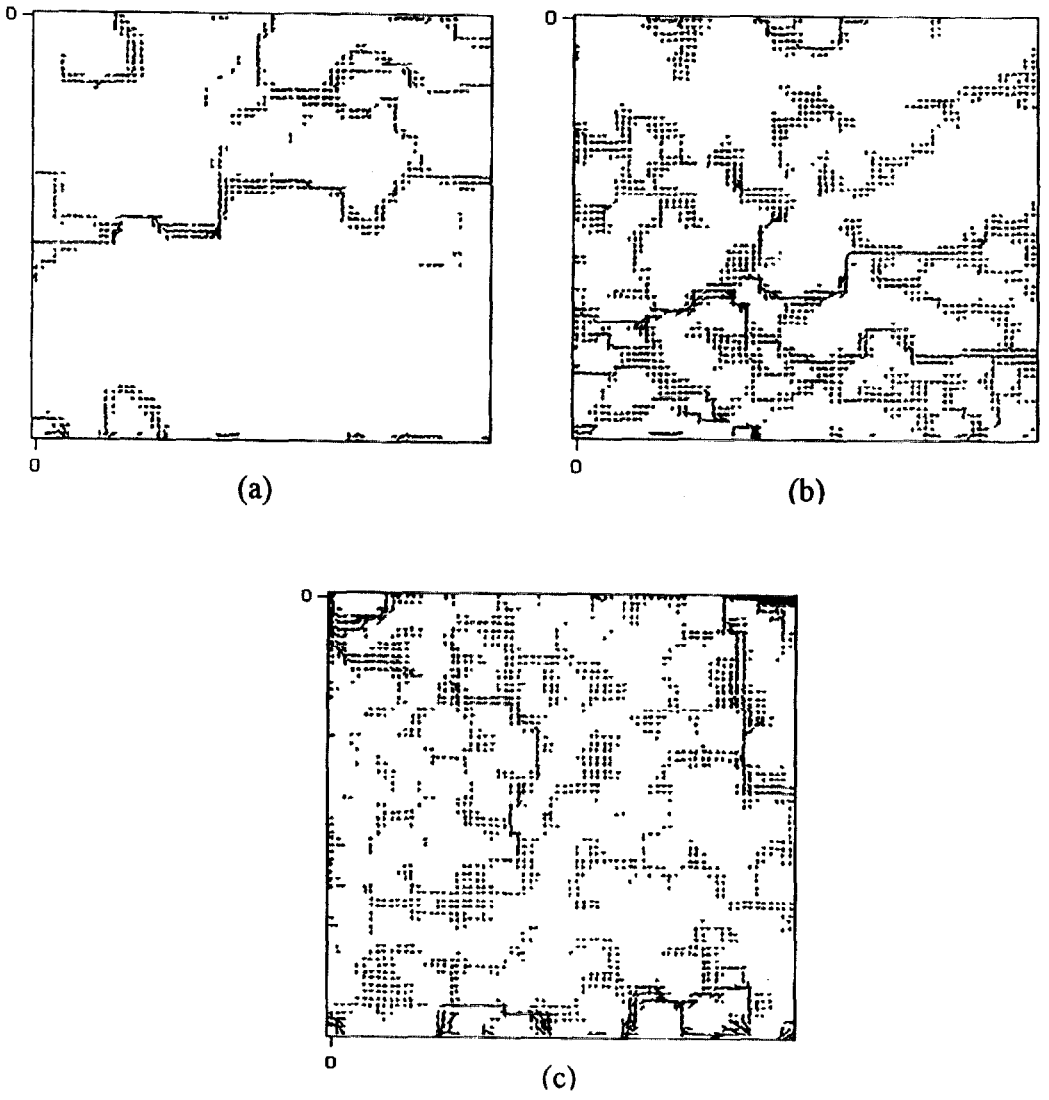

Figure 8. Flow fields in 2-D images of (a) silica sand (porosity of 0.405), (b) Ottawa sand (porosity of 0.396), and (c) glass beads (porosity of 0.393).

K is the symmetric positive definite permeability coefficient tensor. For 2-D analysis of images, (15) can be written as

$$\begin{bmatrix} \bar{u} \\ \bar{v} \end{bmatrix} = -\frac{1}{\mu h}\begin{bmatrix} K_{xx} & K_{xy} \\ K_{yx} & K_{yy} \end{bmatrix}\begin{bmatrix} \Delta p_x \\ \Delta p_y \end{bmatrix}, \tag{16}$$

where $\bar{u}$ and $\bar{v}$ are the average velocity in an image in the x and y directions, respectively. Velocity is measured by an image unit length per second (pixel/second). Here h is the dimension of an image in pixels. The components of the permeability tensor are calculated in two steps. In the first step a pressure difference is applied in the x direction Δp_x, while $\Delta p_y = 0$, and K_{xx} and K_{yx} are calculated as follows:

$$K_{xx} = -\frac{(\mu h) \times \bar{u}}{\Delta p_x} \tag{17}$$

$$K_{yx} = -\frac{(\mu h) \times \bar{v}}{\Delta p_x}. \tag{18}$$

In the second step a pressure difference is applied in the y direction Δp_y, while $\Delta p_x = 0$, and the remaining coefficients of the tensor are calculated as follows:

$$K_{xy} = -\frac{(\mu h) \times \bar{u}}{\Delta p_y} \tag{19}$$

$$K_{yy} = -\frac{(\mu h) \times \bar{v}}{\Delta p_y}. \tag{20}$$

It is noted that the boundary conditions in (10)–(14) are used to solve for fluid flow and calculate the tensor coefficients. The average permeability K_{avg} is the first invariant of the permeability tensor:

$$K_{avg} = \frac{K_{xx} + K_{yy}}{2}. \tag{21}$$

It should be noted that the absolute permeability K has the units of (pixels)^2. It is multiplied by a pixel actual spatial area

Table 1. Comparison of Average Permeability Among Numerical Models and Experimental Values

Source	Ottawa Sand		Silica Sand	Glass Beads	Comments
	Specimen 1	Specimen 2			
Laboratory	92	80	120	200	falling head test
Current study (2-D)	50	37	95	91	using 2-D images of soil microstructure
Current study (3-D)	115	106	122	244	using 3-D simulated soil microstructure
Carman [1946]	20–175				tabulated data (loose beds of sand)
Terzaghi and Peck [1967]	10–100				tabulated data (medium-size clean sands)
Holtz and Kovacs [1981]	1–1000				tabulated data (medium to large-size clean sands)
Kozeny [1927] *Carman* [1956]	202	431	614		

All units are in 10^{-3} cm/s.

$(\Delta x \Delta y)$ to convert it to the units of square meters. The absolute permeability tensor coefficients K are related to Darcy permeability tensor coefficients k with the units of m/s by the following relationship:

$$k = K \frac{\gamma}{\mu}, \tag{22}$$

where $\gamma = 9.81$ kN/m^3 is the fluid (water in this study) unit weight and μ is viscosity and is equal to 10^{-3} kg/(m × s) for water. The permeability coefficients are calculated in the program using the unit of (m/s).

The permeability tensor coefficients and average permeability (equations (17)–(21)) were calculated for images captured on the resin-impregnated specimens. A total of 33 images were analyzed for each of the four specimens of Ottawa sand, silica sand, and glass beads. The average permeability coefficient k_{ave} is reported in Table 1. Since the permeability tensor is symmetric, the values of k_{xy} and k_{yx} were checked for equality. To verify that a symmetric tensor is positive definite, it is sufficient to show that its principal values are positive [*Agnew and Knapp*, 1989]. The principal values of the permeability tensor were calculated using eigenvector analysis and found to be positive. In addition, the directions of major and minor principal values were found to be close to the horizontal and vertical directions, respectively.

Falling head permeability tests were conducted on five replicates of each of the specimens used in the microstructural analysis. That is a total of 20 tests. The average experimental values are reported in Table 1. These values were within a factor of 2.2 of those of the 2-D analysis. The difference of the numerically calculated values from measurements is attributed to two factors. The first one is the limitation of the 2-D analysis in capturing the 3-D pore connectivity. In 3-D media the flow has more paths than the 2-D one. The other factor is the difference in specific surface area between an actual medium and a digital image of that medium. The limited number of pixels on an image alters the specific surface area of smooth particles such as Ottawa sand and glass beads and makes them appear to have rougher surfaces. Increasing the number of pixels in an image can reduce this limitation of using digital images. It would be, however, at the expense of the computational time to calculate the permeability. However, silica sand by nature is composed of rough surface particles, and image digitization would not alter its specific surface area as it does for smooth surface particles. Thus the best agreement between numerically calculated and measured permeability values was found for the silica sand (Table 1).

The program developed by *Martys et al.* [1994] was used to calculate the 3-D permeability values for the simulated soil microstructure presented in section 3. The average permeability values were within a factor of 1.3 of the measured ones (Table 1). This agreement is a further validation of the simulation process of soil microstructure presented in section 3.

Permeability values obtained from tabulated data and empirical relationships for granular materials with porosity and particle size similar to the ones investigated in this study are given in Table 1. It can be seen that the 2-D and 3-D models were within the limits of these values. It is noted, however, that the permeability calculated using the Kozeny-Carman equation [*Kozeny*, 1927; *Carman*, 1956] differed significantly from measured values. The closest prediction by Kozeny-Carman equation yielded a value that varied by about 3.5 times the measured one.

5.2. Permeability Anisotropy Ratio

Permeability anisotropy is measured by the ratio of the horizontal permeability coefficient k_h to the vertical permeability coefficient k_v ($r_k = k_h/k_v$). The anisotropy ratio r_k was determined based on 2-D permeability calculations on 33 images captured on each test specimen. Horizontal permeability was calculated as the average of values measured on horizontal images and in the horizontal direction of vertical images. Vertical permeability was measured on the vertical direction of images. The ratio for the 3-D analysis was calculated by taking the average permeability of the two horizontal directions and dividing by the permeability in the vertical direction. Table 2 shows that the anisotropy ratio was the highest for silica sand. This is expected since silica sand is composed of elongated particles, while Ottawa sand is composed of subrounded particles and glass beads are completely spherical.

The permeability anisotropy for glass beads was higher than unity (Table 2). This was not surprising since permeability anisotropy is controlled by the air void distribution, and several researchers measured a difference in void size between the horizontal and vertical directions of glass bead specimens [*Kallstenius and Bergau*, 1961; *Oda*, 1972; *Masad and Muhunthan*, 2000].

Most of the available measurements of the permeability anisotropy ratio r_k are for cohesive soils and rocks that can be cut and tested in different directions [*Chapuis et al.*, 1989]. Few reliable results are available for cohesionless soils. *Chapuis et al.* [1989] presented laboratory results on the effect of densification methods on the permeability of a cohesionless soil. Results were given for two compaction methods. The permeability anisotropy ratio was lower than 1 (0.87–1.00) for dynamically compacted samples, whereas it was in the 1.33–1.83

Table 2. Values of Permeability Anisotropy Ratio From Numerical Models and Laboratory and Field Tests

Source	Specimens	Permeability Anisotropy Ratio $r_k = k_h/k_v$	Comments
Current study (2-D analysis)	glass beads	1.10	2-D images of soil microstructure
	Ottawa sand (specimen 1)	1.15	
	Ottawa sand (specimen 2)	1.10	
	silica sand	1.30	
Current study (3-D simulation)	glass beads	1.27	3-D simulated soil microstructure
	Ottawa sand (specimen 1)	1.32	
	Ottawa sand (specimen 2)	1.10	
	silica sand	1.67	
Mansur and Dietrich [1965]	granular soil	1.4–4.1 (average = 2.0)	pumping test in the field
Chapuis et al. [1989]	sand	0.87–1.0	dynamically compacted specimens
	sand	1.33–1.83	statically compacted specimens

range for statical compaction. *Mansur and Dietrich* [1965] reported the ratio of horizontal to vertical permeability to vary in the range of 1.4–4.1 with an average of 2.0 based on field pumping tests.

6. Conclusions

A new experimental setup that controls the resin-impregnation time and specimen confinement was used to prepare sand specimens for microstructural analysis. The setup was found to cause very little disturbance to the sand microstructure.

Images of soil microstructure were captured from resin-impregnated specimens with the aid of an optical microscope and an image analysis system. The average porosity and directional autocorrelation function of soil specimens were used to simulate the anisotropic three-dimensional microstructure of sand.

A program was developed for the solution of the two-dimensional Navier-Stokes equations within actual images of soils without a priori assumptions on the significance of viscous or convection (inertial) terms of these equations. Therefore the solution can be used for a wide range of fluid flow applications. The flow equations were solved for materials that differ in porosity, particle size, and specific surface area.

Flow fields were found to be restricted to certain flow paths within an image depending on the size of pores and their connectivity. The number of flow paths decreased with the increase in specific surface area and the decrease in porosity. Flow was found to be more uniformly distributed in glass beads than Ottawa sand and silica sand.

For the test materials the permeability measured in the laboratory was within a factor of 2.2 of the two-dimensional numerically calculated permeability. The model permeability predictions can be further improved by increasing the resolution of images to capture the actual specific surface area of the materials. The numerical 3-D permeability values were within a factor of 1.3 of the measured values.

The permeability anisotropy was found to be correlated with particle elongation. In addition, the permeability anisotropy ratio was in the same range as laboratory and field measurements. These improvements in permeability predictions in comparison with other analytical models are attributed to incorporating the effects of soil microstructure on water flow directly into the solution through boundary conditions. There were no assumptions imposed on the shape of the pore structure.

Appendix

A1. Governing Equations

The finite difference formulations of the governing equations for two-dimensional incompressible flow will be developed by integrating the fundamental differential equations over a control volume using the staggered grid arrangement for the velocity and pressure nodes. The equations will be solved numerically by following the general formulation known as semi-implicit method for pressure linked equations (SIMPLE) [*Patankar and Spalding*, 1970].

A1.1. Continuity equation. Consider a grid system shown in Figure A1a. The continuity cell is centered at the grid point with its sides lying on lines midway between the grid lines. The continuity equation is

$$\frac{\partial \rho u}{\partial x} + \frac{\partial \rho v}{\partial y} = 0. \tag{A1}$$

Integrating this equation over the control volume gives

$$\rho u_e \Delta y - \rho u_w \Delta y + \rho v_n \Delta x - \rho v_s \Delta x = 0 \tag{A2}$$

or

$$G_e - G_w + G_n - G_s = 0, \tag{A3}$$

where n, s, e, and w refer to the north, south, east, and west faces, respectively, of the continuity cell and G_i is the mass flux across the ith face. This is simply the control formulation of the continuity equation for an incompressible flow; the net efflux of mass is zero.

A1.2. Navier-Stokes equations. The momentum equations for incompressible, constant viscosity fluid flow are given by the Navier-Stokes equations. The control volume used for the momentum equation in x direction is shown as the patterned area in Figure A1b. The control volume lies between the $n' - s'$ and the $w' - e'$ grid lines. The u velocity node lies at the center of the x-momentum cell. The pressure nodes lie at the grid nodes. This constitutes the staggered grid arrangement.

The momentum equation for a steady, incompressible flow in the x direction is

$$\frac{\partial}{\partial x}\left(\rho u u - \mu \frac{\partial u}{\partial x}\right) + \frac{\partial}{\partial y}\left(\rho u v - \mu \frac{\partial u}{\partial y}\right) = -\frac{\partial p}{\partial x} + \frac{\partial}{\partial x}\left(\mu \frac{\partial u}{\partial x}\right) + \frac{\partial}{\partial y}\left(\mu \frac{\partial v}{\partial x}\right). \tag{A4}$$

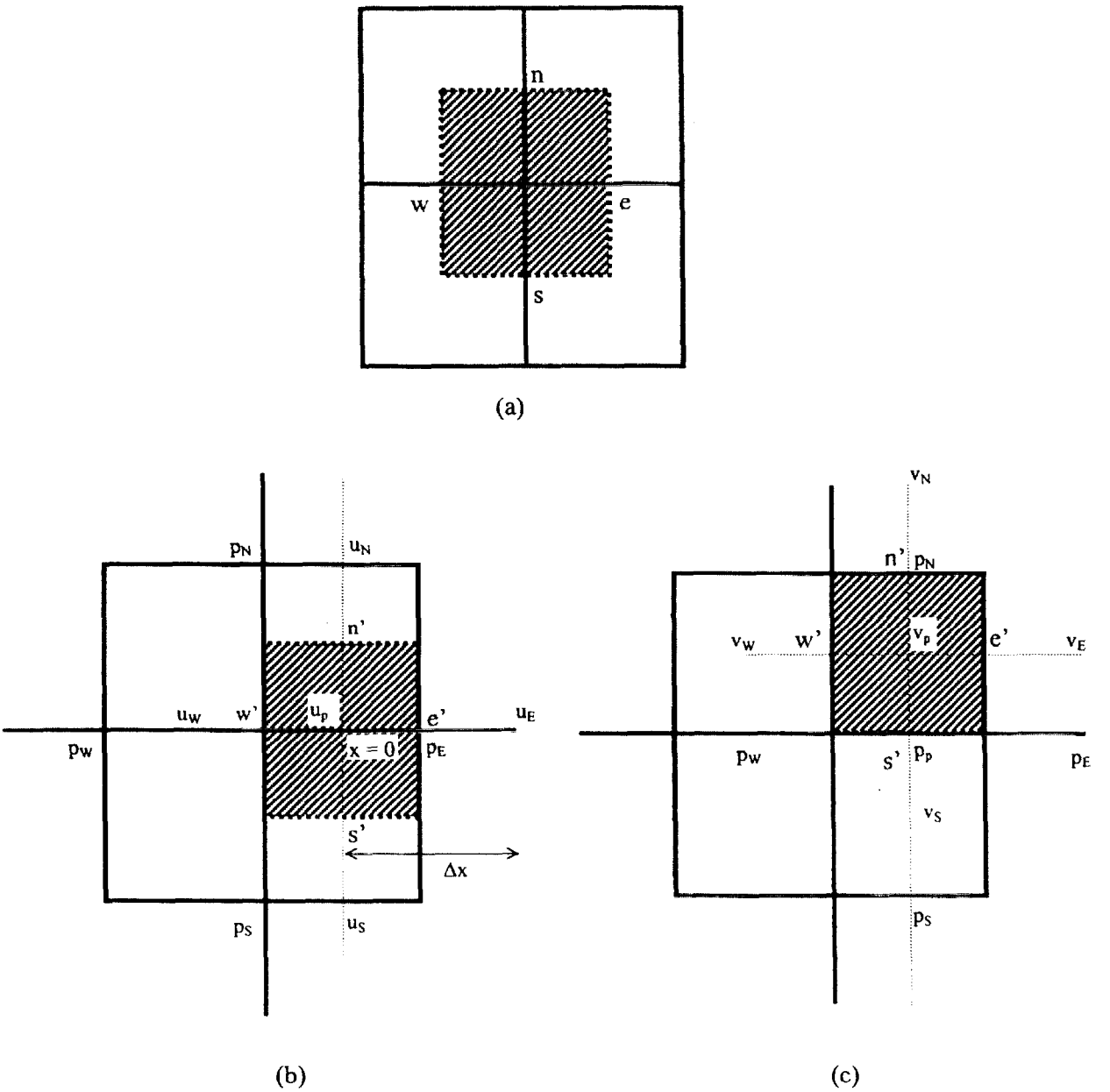

Figure A1. Arrangement of the continuity and momentum cells on the staggered grid: (a) continuity cell, (b) momentum cell in x direction, and (c) momentum cell in y direction.

Integrating this equation over the volume of the momentum cell results in

$$\left(\rho uu - \mu \frac{\partial u}{\partial x}\right)_{e'} \Delta y - \left(\rho uu - \mu \frac{\partial u}{\partial x}\right)_{w'} \Delta y + \left(\rho uv - \mu \frac{\partial u}{\partial y}\right)_{n'} \Delta x - \left(\rho uv - \mu \frac{\partial u}{\partial y}\right)_{s'} \Delta x = (p_{w'} - p_{e'})\Delta y + \left(\mu \left.\frac{\partial u}{\partial x}\right|_{e'} - \mu \left.\frac{\partial u}{\partial x}\right|_{w'}\right)\Delta y + \left(\mu \left.\frac{\partial v}{\partial x}\right|_{n'} - \mu \left.\frac{\partial v}{\partial x}\right|_{s'}\right)\Delta x. \quad \text{(A5)}$$

This first term of (A5) is the momentum flux in the x direction on the east face of the momentum cell. This term is denoted $M^x_{e'}$, and it can be written in terms of the mass flux on the east face ($G_{e'}$) as

$$M^x_{e'} = G_{e'}u - \mu \left.\frac{\partial u}{\partial x}\right|_{e'} \Delta y. \quad \text{(A6)}$$

Approximating the partial derivative with a total derivative and integrating this equation yields

$$u = \frac{M^x_{e'}}{G_{e'}} + Ce^{[(G_{e'}x)/(\mu\Delta y)]}, \quad \text{(A7)}$$

where C is the constant of integration. Consider the x component of velocities in the neighborhood of the east face of the

momentum cell shown in Figure A1b. At $x = 0$ the velocity is equal to the velocity at the center of the momentum cell, namely, u_p. At a distance Δx from the cell center is the velocity at the center of the adjacent cell or the east velocity u_E. Applying these boundary conditions and solving for the momentum flux on the east face results in

$$M^x_{e'} = G_{e'} \frac{u_E - u_p e^{Re_c}}{1 - e^{Re_c}}. \tag{A8}$$

The exponent of the exponential term is the cell Reynolds number $Re_c = (G_{e'}x)/(\mu\Delta y)$. The momentum flux in the x direction across the east face (equation (A8)) can be expressed as

$$M^x_{e'} = G_{e'}[f_{e'}u_E + (1 - f_{e'})u_p], \tag{A9}$$

where for $|Re_c| \gg 1$, $f_{e'} = 0$ if $G_{e'} \geq 0$ or $f_{e'} = 1$ if $G_{e'} < 0$, and for $|Re_c| \ll 1$, $f_{e'} = \frac{1}{2} - [\mu/(\rho u_{e'}\Delta x)]$.

Similar equations can be written for the x-momentum flux across the other faces. Combining all the momentum fluxes into the finite difference equation, (A5), results in the following equation:

$$\begin{aligned}(G_{e'} - G_{w'} + G_{n'} - G_{s'})u_p + (-f_{e'}G_{e'} - f_{n'}G_{n'} + f_{w'}G_{w'} + f_{s'}G_{s'})u_p \\ + f_{e'}u_E G_{e'} + f_{n'}u_N G_{n'} - f_{w'}u_W G_{w'} - f_{s'}u_S G_{s'} \\ = (p_p - p_E)\Delta y + S_{\text{visc}},\end{aligned} \tag{A10}$$

where S_{visc} is the term that appears because the viscosity is not uniform [*Masad*, 1998]. For uniform viscosity and incompressible flow this term is zero. Further, the first term in (A10) is zero because of the continuity equation. Defining the coefficients of the velocities as

$$a_{e'} = f_{e'}G_{e'} \tag{A11}$$

$$a_{w'} = f_{w'}G_{w'} \tag{A12}$$

$$a_{s'} = f_{s'}G_{s'} \tag{A13}$$

$$a_{n'} = f_{n'}G_{n'}, \tag{A14}$$

the momentum equation (A10) can be written in a compact from:

$$u_p \sum_{i=n,e,s,w} a_{i'} = \sum_{\substack{i=n,e,s,w \\ j=N,E,S,W}} a_{i'}u_j + (p_p - p_E)\Delta y + S_{\text{visc}}. \tag{A15}$$

At this point, another term $S_p u_p$ is added to (A15) which is a function of the boundary conditions as will be shown later in this appendix. Hence (A15) becomes

$$u_p = \frac{\sum_{\substack{i=n,e,s,w \\ j=N,E,S,W}} a_{i'}u_j}{a_{p'}} + \frac{(p_p - p_E)\Delta y}{a_{p'}} + \frac{S_{\text{visc}}}{a_{p'}}, \tag{A16}$$

where $a_{p'} = \Sigma_{i=n,e,s,w} a_{i'} - S_p$.

Following the above steps for the momentum equation in the y direction (Figure A1c), the momentum equation in y direction becomes

$$v_p = \frac{\sum_{\substack{i=n,e,s,w \\ j=N,E,S,W}} a_{i'}v_j}{a_{p'}} + \frac{(p_p - p_N)\Delta x}{a_{p'}} + \frac{S_{\text{visc}}}{a_{p'}}. \tag{A17}$$

A2. Pressure Formulation of Continuity Equation

The finite difference equation for the velocity on the east face of the continuity cell (Figure A1a) can be expressed using the x-momentum equation as

$$u_e = \frac{\sum_{\substack{i=n,e,s,w \\ j=N,E,S,W}} a_i u_j}{a_{p,e}} + \frac{(p_p - p_E)\Delta y}{a_{p,e}} + \frac{S_{\text{visc}}}{a_{p,e}}, \tag{A18}$$

where $a_{p,e}$ is the coefficient for the velocity on the east face of the continuity cell and the center of the momentum cell. the change in the velocity due to a change in pressure can be approximated through the first terms of a Taylor series expansion:

$$u_e = u_e^o + \frac{\partial u_e}{\partial p_p}(\Delta p_p) + \frac{\partial u_e}{\partial p_E}(\Delta p_E), \tag{A19}$$

where $\Delta p_p = p_p - p_p^o$ is the pressure change, and u_e^o and p_p^o are the velocity and pressure values from the previous iteration, respectively. Substituting for the partial derivatives of u_e in (A19) from (A18) gives

$$u_e = u_e^o + \frac{\Delta y}{a_{p,e}}(\Delta p_p) - \frac{\Delta y}{a_{p,e}}(\Delta p_E). \tag{A20}$$

Similar equations can be written for the three remaining faces. Substituting these equations into the continuity equation (A2) results in the following equation for the pressure change:

$$\bar{a}_p \Delta p_p = \sum_{i=N,S,E,W} \bar{a}_i \Delta p_i - \sum_{i=n,s,e,w} G_i, \tag{A21}$$

where

$$\bar{a}_p = \rho\Delta y^2 \left(\frac{1}{a_{p,e}} + \frac{1}{a_{p,w}}\right) + \rho\Delta x^2 \left(\frac{1}{a_{p,n}} + \frac{1}{a_{p,s}}\right) \tag{A22}$$

$$\bar{a}_E = \frac{\rho\Delta y^2}{a_{p,e}} \tag{A23}$$

$$\bar{a}_W = \frac{\rho\Delta y^2}{a_{p,w}} \tag{A24}$$

$$\bar{a}_N = \frac{\rho\Delta x^2}{a_{p,n}} \tag{A25}$$

$$\bar{a}_S = \frac{\rho\Delta x^2}{a_{p,s}}. \tag{A26}$$

A3. Boundary Conditions

The flow equations are solved for actual images of the soil microstructure. Velocity fields within an image are driven by a pressure difference $\Delta p = p_2 - p_1$ maintained between the inlet and the outlet of an image (Figure 7). The boundary conditions of velocity components are

$$u(x = 0) = u(x = h) \tag{A27}$$

$$v(x = 0) = v(x = h) \tag{A28}$$

$$u(y = 0) = u(y = h) \tag{A29}$$

$$v(y = 0) = v(y = h) \tag{A30}$$

and at the solid phase ("no slip" condition)

$$u = v = 0, \tag{A31}$$

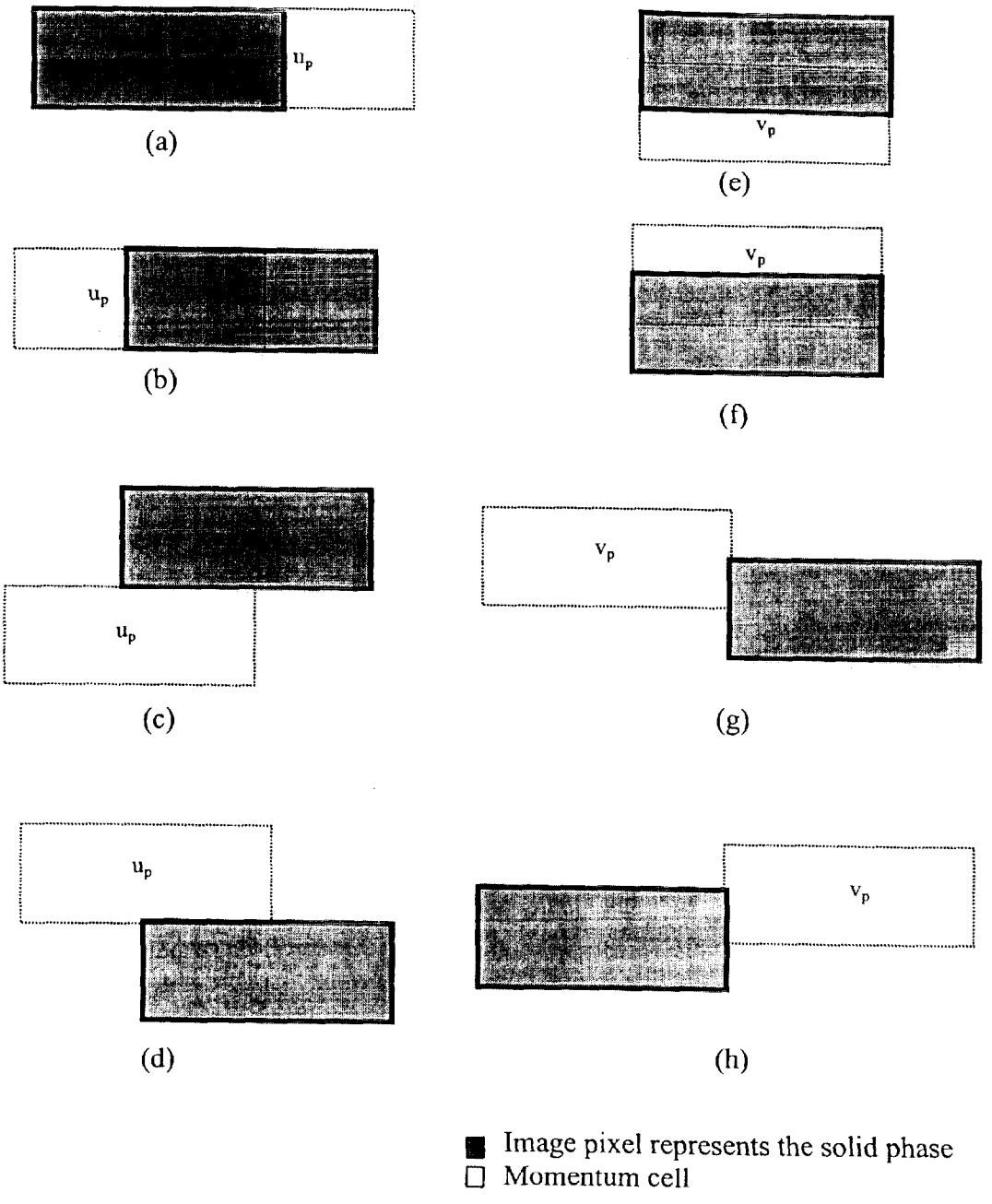

Figure A2. The effect of "no slip" boundary condition on the momentum equation coefficients.

where u and v are the velocity components at any point of an image in the x and y directions, respectively, and h is the width of an image in pixels. Equations (A27)–(A31) represent periodic boundary conditions. The momentum coefficients in (A11)–(A14) are calculated to conform with the "no slip" boundary condition in (A31). Figure A2 shows possible contact configurations between a momentum cell and solid cells, and Table A1 lists the correspondent values of momentum coefficients [*Masad*, 1998].

As mentioned earlier in this appendix, S_p value is also a function of the boundary conditions of a momentum cell. Table A1 presents the S_p values as they relate to the contact configurations with solid cells. It should be noticed that when the velocity at the center of the momentum cell coincides with the solid wall (Figures A2a, A2b, A2e, and A2f), the velocity value at the wall should be equal to zero. In order to comply with this condition, a_p coefficient in (A16) should be equal to a very large value, and hence a very large value is assigned to S_p.

A4. Solution Scheme

The solution scheme for the finite difference formulations consists of the following steps: (1) Assume velocity and pressure field within an image. (2) Solve the momentum equations for the velocities at the internal nodes. (3) Using these velocities, evaluate the source term for the pressure formulation of the continuity equation (A21). If the continuity residuals satisfy the convergence criterion, terminate the calculations. The criterion used for convergence is usually

Table A1. Momentum Equations Coefficients at Different Boundary Conditions

Contact Configuration	a_e	a_w	a_s	a_n	S_p
No contact with solid cells	$-\frac{1}{2}\rho u_e \Delta y + \mu \frac{\Delta y}{\Delta x}$	$\frac{1}{2}\rho u_w \Delta y + \mu \frac{\Delta y}{\Delta x}$	$\frac{1}{2}\rho v_s \Delta x + \mu \frac{\Delta x}{\Delta y}$	$-\frac{1}{2}\rho v_n \Delta x + \mu \frac{\Delta x}{\Delta y}$	zero
Figure A2a	$-\frac{1}{2}\rho u_e \Delta y + \mu \frac{\Delta y}{\Delta x}$	$\mu \frac{\Delta y}{\Delta x}$	$\frac{1}{4}\rho v_s \Delta x + \frac{1}{2}\mu \frac{\Delta x}{\Delta y}$	$-\frac{1}{4}\rho v_n \Delta x + \frac{1}{2}\mu \frac{\Delta x}{\Delta y}$	very large
Figure A2b	$\mu \frac{\Delta y}{\Delta x}$	$\frac{1}{2}\rho u_w \Delta y + \mu \frac{\Delta y}{\Delta x}$	$\frac{1}{4}\rho v_s \Delta x + \frac{1}{2}\mu \frac{\Delta x}{\Delta y}$	$-\frac{1}{4}\rho v_n \Delta x + \frac{1}{2}\mu \frac{\Delta x}{\Delta y}$	very large
Figure A2c	$-\frac{1}{2}\rho u_e \Delta y + \mu \frac{\Delta y}{\Delta x}$	$\frac{1}{2}\rho u_w \Delta y + \mu \frac{\Delta y}{\Delta x}$	$\frac{1}{2}\rho v_s \Delta x + \mu \frac{\Delta x}{\Delta y}$	$-\frac{1}{4}\rho v_n \Delta x + \frac{1}{2}\mu \frac{\Delta x}{\Delta y}$	$-\frac{1}{2}\mu \frac{\Delta y}{\Delta x}$
Figure A2d	$-\frac{1}{2}\rho u_e \Delta y + \mu \frac{\Delta y}{\Delta x}$	$\frac{1}{2}\rho u_w \Delta y + \mu \frac{\Delta y}{\Delta x}$	$\frac{1}{4}\rho v_s \Delta x + \frac{1}{2}\mu \frac{\Delta x}{\Delta y}$	$-\frac{1}{2}\rho v_n \Delta x + \mu \frac{\Delta x}{\Delta y}$	$-\frac{1}{2}\mu \frac{\Delta y}{\Delta x}$
Figure A2e	$-\frac{1}{4}\rho u_e \Delta y + \frac{1}{2}\mu \frac{\Delta y}{\Delta x}$	$\frac{1}{4}\rho u_w \Delta y + \frac{1}{2}\mu \frac{\Delta y}{\Delta x}$	$\frac{1}{2}\rho v_s \Delta x + \mu \frac{\Delta x}{\Delta y}$	$\mu \frac{\Delta x}{\Delta y}$	very large
Figure A2f	$-\frac{1}{4}\rho u_e \Delta y + \frac{1}{2}\mu \frac{\Delta y}{\Delta x}$	$\frac{1}{4}\rho u_w \Delta y + \frac{1}{2}\mu \frac{\Delta y}{\Delta x}$	$\mu \frac{\Delta x}{\Delta y}$	$-\frac{1}{2}\rho v_n \Delta x + \mu \frac{\Delta x}{\Delta y}$	very large
Figure A2g	$-\frac{1}{4}\rho u_e \Delta y + \frac{1}{2}\mu \frac{\Delta y}{\Delta x}$	$\frac{1}{2}\rho u_w \Delta y + \mu \frac{\Delta y}{\Delta x}$	$\frac{1}{2}\rho v_s \Delta x + \mu \frac{\Delta x}{\Delta y}$	$-\frac{1}{2}\rho v_n \Delta x + \mu \frac{\Delta x}{\Delta y}$	$-\frac{1}{2}\mu \frac{\Delta x}{\Delta y}$
Figure A2h	$-\frac{1}{2}\rho u_e \Delta y + \mu \frac{\Delta y}{\Delta x}$	$\frac{1}{4}\rho u_w \Delta y + \frac{1}{2}\mu \frac{\Delta y}{\Delta x}$	$\frac{1}{2}\rho v_s \Delta x + \mu \frac{\Delta x}{\Delta y}$	$-\frac{1}{2}\rho v_n \Delta x + \mu \frac{\Delta x}{\Delta y}$	$-\frac{1}{2}\mu \frac{\Delta x}{\Delta y}$

$$\sum |G_i| \leq \varepsilon, \tag{A32}$$

where the summation is performed over all the computational cells. (4) Solve the pressure equation for the pressure change. (5) Correct the velocities and pressures with the calculated pressure change (for example, by using (A20) for the east face and similar equations for velocities in other faces and by adding the pressure change to the previous pressure). (6) Update the velocities at the external nodes using the periodic boundary condition. (7) Return to step 2 and continue until convergence in step 3 is achieved. The tridiagonal matrix algorithm is used to solve the sets of equations in steps 2 and 4. When solving for the velocity components in momentum equations and pressure changes in the continuity equation, the solution of an iteration may sometimes experience convergence problems in terms of slow convergence or divergence. This problem can be solved by incorporating a relaxation factor in the original equation [*Masad*, 1998].

Notation

$f_r(l)$ the spherical harmonics series formulation of the directional autocorrelation function (ACF).
h image width in pixels.
k Darcy's permeability coefficient.
K absolute permeability coefficient.
$\mathbf{I}$ unit vector.
n average axial ratio.
r vector length used in the directional ACF analysis.
$\bar{u}$ average velocity in x direction.
v average velocity in z direction.
$\mathbf{v}$ average fluid velocity vector.
∇p pressure gradient.
ρ fluid density.
μ fluid viscosity.
γ fluid unit weight.
Ω ACF tensor.
Ω_{mn} ACF tensor component.

Acknowledgment. The study presented in this paper was sponsored by the National Science Foundation under grant CMS-9309345 to Washington State University.

References

Adler, P. M., C. G. Jacquin, and J. A. Quiblier, Flow in simulated porous media, *Int. J. Multiphase Flow*, *16*(4), 691–712, 1990.

Agnew, J. L., and R. C. Knapp, *Linear Algebra With Applications*, Books/Cole, Pacific Grove, Calif., 1989.

Bear, J., *Dynamics of Fluids in Porous Media*, Elsevier Sci., New York, 1972.

Berryman, J. G., and S. C. Blair, Use of digital image analysis to estimate fluid permeability of porous materials: Application of two-point correlation functions, *J. Appl. Phys.*, *60*, 1930–1938, 1986.

Bird, R. B., W. E. Stewart, and E. N. Lightfoot, *Transport Phenomena*, John Wiley, New York, 1960.

Carman, P. C., *Flow of Gases Through Porous Media*, Academic, San Diego, Calif., 1956.

Chapuis, R. P., D. E. Gill, and K. Bass, Laboratory permeability tests on sand: Influence of the compaction method on anisotropy, *Can. Geotech. J.*, *26*, 614–622, 1989.

Childs, E. C., and N. Collis-George, The permeability of porous materials, *Proc. R. Soc. London, Ser. A*, *201*, 392–405, 1950.

Dullien, F. A. L., *Porous Media Fluid Transport and Pore Structure*, Academic, San Diego, Calif., 1979.

Holtz, R. D., and D. K. Kovacs, *An Introduction to Geotechnical Engineering*, Prentice-Hall, Englewood Cliffs, N. J., 1981.

Ibrahim, A., and T. Kagawa, Microscopic measurement of sand fabric from cyclic tests causing liquefaction, *Geotech. Test. J.*, *14*(4), 371–382, 1991.

Kallstenius, T., and W. Bergau, Research on the structure of granular masses, *Proc. Fifth Int. Conf. Soil Mech. Found. Eng. 5th*, *1*, 165–170, 1961.

Koplic, J., C. Lin, and M. Vermette, Conductivity and permeability from microgeometry, *J. Appl. Phys.*, *56*, 3127–3131, 1984.

Kozeny, J., Über Kapillare Leitung des Wassers im Boden, *Wien Akad. Wiss.*, *136*(2A), 271, 1927.

Kuo, C. Y., and J. D. Frost, Quantifying the fabric of granular materials–An image analysis approach, *Rep. GIT-CEE/GEO-95-1*, Dep. of Civ. and Environ. Eng., Ga. Inst. of Technol., Atlanta, Ga., 1995.

Law, A. M., and W. D. Kelton, *Simulation Modeling and Analysis*, McGraw-Hill, New York, 1982.

Mansur, C. I., and R. S. Dietrich, Pumping tests to determine permeability ratio, *J. Soil Mech. Found. Div. Am. Soc. Civ. Eng.*, *91*(SM4), 151–183, 1965.

Martys, N. S., S. Torquato, and D. P. Bentz, Universal scaling of fluid permeability for sphere packings, *Phys. Rev. E*, *50*, 403–408, 1994.

Masad, E., Permeability simulation of reconstructed anisotropic soil medium, Ph.D. thesis, Wash. State Univ., Pullman, 1998.

Masad, E., and B. Muhunthan, Simulation of three-dimensional anisotropic soil microstructure, in *Imaging Technologies: Techniques and Applications in Civil Engineering*, edited by S. McNeil and D. Frost, pp. 265–285, Am. Soc. of Civ. Eng., Reston, Va., 1998.

Masad, E., and B. Muhunthan, Three-dimensional characterization and simulation of anisotropic soil structure, *J. Geotech. Geoenviron. Eng.*, *126*(3), in press, 2000.

Miura, S., and S. Toki, A sample preparation method and its effect on static and cyclic deformation strength properties of sand, *Soils Found.*, *22*(1), 61–77, 1982.

National Institutes of Health, *Software Program "Image,"* version 1.57, Bethesda, Md., 1992.

Oda, M., Initial fabrics and their relations to mechanical properties of granular material, *Soils Found.*, *12*(1), 17–36, 1972.

Patankar, S. V., and D. B. Spalding, A calculation procedure for heat, mass and momentum transfer in three-dimensional parabolic flows, *Int. J. Heat Mass Transfer*, *15*, 1787–1806, 1970.

Press, W. H., and S. A. Teukolsky, Portable random number generators, *Comput. Phys.*, *6*(5), 522–524, 1992.

Smart, P., and N. K. Tovey, *Electron Microscopy of Soils and Sediments: Techniques*, Oxford Sci., London, 1982.

Terzaghi, K., and R. B. Peck, *Soil Mechanics in Engineering Practice*, John Wiley, New York, 1967.

N. Martys, Building and Fire Research Laboratory, National Institute of Standards and Technology, Building 226, Room B-348, Gaithersburg, MD 20899. (martys@cam.nist.gov)

E. Masad and B. Muhunthan, Department of Civil and Environmental Engineering, Washington State University, P.O. Box 642910, Pullman, WA 99164-2910. (masad@wsu.edu; muhuntha@wsu.edu)

(Received March 18, 1999; revised December 6, 1999; accepted December 8, 1999.)